Gas-flow distribution in bubbling fluidized beds: CFD-based analysis and impact of operating conditions

As Published: 10.1016/J.POWTEC.2017.01.005

Publisher: Elsevier BV

Persistent URL: https://hdl.handle.net/1721.1/134480

Version: Author's final manuscript: final author's manuscript post peer review, without publisher's formatting or copy editing

Gas-Flow Distribution in Bubbling Fluidized Beds: CFD-Based Analysis and Impact of Operating Conditions

A. Bakshi[a,*], C. Altantzis[a,b], L.R. Glicksman[a], A.F. Ghoniem[a]

[a] *Massachusetts Institute of Technology, Department of Mechanical Engineering*
77 Massachusetts Ave., Cambridge, MA 02139, USA
[b] *National Energy Technology Laboratory, Morgantown, WV 26507, USA*

Abstract

Gas-flow distribution plays a critical role in the performance of fluidized beds because it directly affects gas residence-time and solids mixing. However, measuring it accurately in the harsh conditions of larger reactors is not possible. Therefore, this study is focused on the development of a rigorous computational framework for quantifying gas-flow distribution during fluidization. To this end, fine-grid simulations are conducted for the bubbling fluidization of two distinct Geldart B particles- 1.15 mm LLDPE and 0.50 mm glass particles, at superficial gas velocities U/U_{mf}=2 and 3 in a 50 cm diameter bed. The Two-Fluid Model (TFM) is employed to describe the solids motion efficiently and in-house developed tool MS3DATA (Multiphase-flow Statistics using 3D Detection and Tracking Algorithm) to compute detailed bubble statistics. The overall gas flow is divided into three phases: (a) dense flow in areas relatively rich is solids concentration (b) "visible" bubble flow associated with rising bubbles and (c) throughflow accounting for the gas flow which mostly bypasses through bubbles. It is found that conditions within the dense-phase depend largely on the particle properties while bubbling dynamics are significantly affected by superficial gas velocity. Calculations show that the throughflow increases in areas frequented by bubbles because the voidage distribution around bubbles increases the local dense-phase permeability. Throughflow may account for up to 40% of the overall gas flow, especially in the fluidization of large particles. This is not desirable because its residence-time is almost 2× shorter (as compared to the dense flow) and contributes minimally to solids mixing. Finally, it is shown that in comparison to lab-scales, larger beds exhibit more homogeneous gas mixing. Insights from this study and the methodology developed will be useful in investigating gas flow distribution in complex fuel conversion systems.

Keywords: Fluidized beds, Two-Fluid Model, gas distribution, bubble dynamics, throughflow

1. Introduction

Fluidized beds are widely used in the chemical and petroleum industries, because of their high heat and mass transfer rates resulting from large gas-solids contacting [1]. However, design and performance optimization of commercial-scale fluidized beds continues to be challenging because of limitations of diagnostic techniques in the harsh conditions most fluidized beds operate in. Recently, there has been considerable progress in multiscale, multiphase modeling based on Computational Fluid Dynamics (CFD), which can accurately simulate local and global fluidization hydrodynamics and hence, can be used to investigate different physical and chemical phenomena occurring in these systems. This study is focused on developing a framework for describing the bubbling dynamics and gas-flow distribution, using fine-grid CFD simulations.

Distribution of gas flow in fluidized beds adversely affects gas residence time and solids mixing [1, 37–39], and therefore, impacts bed reactor's operation and performance. Recognizing this, substantial experimental and analytical effort have been undertaken to describe gas flow accurately and reliably [2–6]. The *two-phase* theory first proposed by Toomey and Johnstone [7] was based on the premise that the dense phase (or emulsion) is minimally fluidized (at U_{mf}) while the excess gas (= U-U_{mf}) flows through rising bubbles. Subsequent experimental measurements indicated that this theory grossly overestimates the visible bubble flow and demonstrated that a significant fraction of the gas bypasses through bubbles, especially in the fluidization of Geldart B and D particles [1, 2]. To account for the bypassed gas, commonly referred to as through-flow, modifications to

*Corresponding Author
Email address: abakshi@mit.edu, Telephone number: +1 (617) 253-5365

this theory were proposed (most notably the n-type theory [2]), all of which are based on the division of the gas flow into three components: (a) gas contributing to the dense phase (with axial velocity U_d) (b) "visible" bubble flow Q_b and (c) throughflow (with axial velocity U_{tf}) which, at steady state, can be related by volume conservation at any axial location:

$$UA = (1 - \delta)U_d A + Q_b + \delta U_{tf} A \tag{1}$$

where U is the superficial gas velocity, A is the cross-sectional area of the bed and δ is the bubble fraction (fraction of cross-sectional area occupied by bubbles). From their experiments using thin rectangular fluidized beds, Grace and Harrison [2] suggested that U_d can be approximated as U_{mf}; this was later corroborated by the analytical modeling of Valenzuela and Glicksman [4] for large (Geldart B) particles. Additionally, they suggested that U_d must not depend on bubble characteristics and is, therefore, independent of the superficial gas velocity.

Meanwhile, visible bubble flow Q_b, which is the gas-flow associated with rising bubbles, has been conventionally quantified using cine photography and high speed video in thin-rectangular beds (e.g. [2, 8]) or probes (fiber optic or capacitance) in 3D beds [9, 10]. Despite considerable uncertainty associated with bubble measurements, it is generally established that Q_b is sensitive to both bed geometry and operating conditions. Inferences from thin-rectangular beds may not be applicable to real cylindrical bed systems because the hydrodynamics are significantly affected by the close proximity of walls in the spanwise direction [11, 12]. Further, in lab-scale beds, large bubbles and slugs are frequently observed which is not the case in relatively larger beds, where bubbles laterally coalesce towards the center over considerable axial distance resulting in significantly different solids circulation patterns [10, 13]. On the other hand, particle properties directly affect bubble structure: fluidization of small Geldart A particles is characterized by fast bubbles associated with clouds separating gas flow within bubbles from the dense-phase. In case of larger particles (Geldart B and D), the interstitial gas (through the dense-phase) is faster than the speed of typical bubble rise and is, therefore, able to bypass through bubbles [6].

Throughflow is frequently observed in large-particle systems and constitutes the component of gas flow that escapes into the freeboard through swarms of bubbles which offer low-resistance pathways. This results in minimal interaction with the dense-phase and adversely affects mixing of solid particles. Therefore, quantifying throughflow is critical for analyzing bed reactor performance and optimization, but direct measurement is not possible because of limitations in diagnostic techniques. Most studies (e.g. [3, 4, 6, 14–16]) have estimated throughflow indirectly, based on bubble measurements and assumptions regarding the dense-phase, while only recently [17, 18], attempts have been made to characterize throughflow using detailed analysis of experimental and numerical data. While the methodologies prescribed by the latter studies are useful for investigating throughflow fundamentally, their conclusions are based on observations in thin rectangular beds (where walls in the spanwise direction significantly impact fluidization hydrodynamics) and therefore, cannot be extrapolated to larger 3D fluidized beds [13, 19]. Overall, throughflow is expected to increase in areas of high coalescence activity, which are usually correlated with high density of small bubbles.

Given the chaotic nature of the interactions and the complex physical phenomena associated with bubbling fluidization, it is not surprising that a generalized description of the gas flow across a range of bed sizes and operating conditions has not been possible. This challenge is further exacerbated by technical limitations with simultaneous measurements of the dense and bubble phases. In cylindrical beds, measurements based on point probes (fiber-optic and capacitance) require assumptions regarding bubble shape and trajectory while accurate quantification using more sophisticated techniques (e.g. γ- and X-Ray imaging) is only possible in lab-size beds and at low bubble fraction (<0.1) [4, 8]. Thus, highly resolved CFD simulations can provide valuable insights into the bubbling behavior and gas distribution, and the developed framework can be employed in modeling different systems.

This work is part of a series of studies investigating bubbling fluidization of Geldart B particles. In [19–21], the computational framework and suitable metrics were developed to validate critical sub-models at the lab-scale. For predicting bubbling dynamics at large-scales, MS3DATA (Multiphase-flow Statistics using 3D Detection and Tracking Algorithm) was developed in [22] which uses time-resolved volumetric void fraction data from simulations. In [13], the effect of reactor size (bed diameter D and initial bed height H_0) on the fluidization hydrodynamics was examined using fine-grid CFD simulations and predictions were analyzed qualitatively using time-resolved visualization, bubble centroid and solids velocity vector maps and quantitatively using detailed bubble statistics and solids circulation metrics. Overall, it was shown that (a) scalability of predictions is only possible when bubble size and spatial distributions are consistent across scales (initial bed height must be lower than the critical height for gulf-stream circulations) and (b) for fluidization of Geldart B particles, predictions

in a 50 cm diameter bed are reasonably independent of bed size.

This study is focused on developing a rigorous framework for describing gas-flow distribution in bubbling fluidized beds. To this end, simulations are conducted for the fluidization of two distinct particles (1.15 mm LLDPE and 0.5 mm glass) at superficial gas velocities U/U_{mf}=2 and 3 in 15-70 cm diameter beds. Observations and insights are also compared with previous modeling efforts and experimental evidence. The simulation setup and fluidization metrics (phase-specific statistics) are first discussed briefly in Sections 2 and 3, respectively. Next, the computational framework for gas-flow distribution is detailed for the fluidization of LLDPE particles at U/U_{mf}=2 and 3 in Sections 4.1-4.4. Finally, the effects of particle properties and reactor size are analyzed in Sections 4.5 and 4.6, respectively. All simulations are performed using MFiX (Multiphase Flow with Interface eXchanges) [23, 28], an open-source code developed at the National Energy Technology Laboratory, USA to describe the hydrodynamics in solid-gas systems.

2. Simulation Setup

The simulation framework for all analyses conducted in this study is presented in [13] where the impact of bed size on fluidization hydrodynamics was analyzed to establish that (a) the initial bed height H_0 does not significantly affect fluidization hydrodynamics, (b) larger beds (> 50 cm diameter) are characterized by smaller bubbles and faster solids axial circulation (compared to lab-scale beds) and (c) dynamics in beds larger than 50 cm diameter are weakly dependent on the bed diameter. Based on these conclusions, analysis of gas distribution in this study is focused on the fluidization of two Geldart B particles (500 μm glass and 1150 μm LLDPE) in a fluidized bed of diameter 50 cm and initial bed aspect ratio ($H_0/D = 1$), and the effect of superficial gas velocity and scale are also investigated. Key aspects regarding the simulation setup are discussed below while further details can be found in [13].

2.1. Governing Equations

Several modeling frameworks have been employed for simulating solid-gas flow with varying degrees of physical resolution (see [36] and references therein). Simulations presented in this study are based on the Two-Fluid model which balances accuracy and computational cost at relatively large-scales by representing the gas and solid phases as inter-penetrating continua. For cold fluidization, the transport equations for mass and momentum reduce to

$$\frac{\partial}{\partial t}\left(\varepsilon_k \rho_k\right) + \nabla \cdot \left(\varepsilon_k \rho_k \vec{V}_k\right) = 0 \tag{2}$$

$$\frac{\partial}{\partial t}\left(\varepsilon_k \rho_k \vec{V}_k\right) + \nabla \cdot \left(\varepsilon_k \rho_k \vec{V}_k \vec{V}_k\right) = \nabla \cdot \bar{\bar{S}}_k - \varepsilon_k \nabla P_g + \varepsilon_k \rho_k \vec{g} + \left(\delta_{km}\vec{I}_{gm} - \delta_{kg}\vec{I}_{gm}\right) \tag{3}$$

$$\delta_{ki} = \begin{cases} 1 & \text{if } k = i \\ 0 & \text{otherwise} \end{cases} \tag{4}$$

where ε, ρ and $\vec{V}$ are the volume fraction, density and velocity for the gas ($k = g$) and solid ($k = m$) phases. The solids stress tensor $\bar{\bar{S}}_m$ is evaluated using the Kinetic Theory of Granular Flow (KTGF) [23] in dilute regions where collisional forces are relatively dominant and Shaeffer's theory [24] in dense pockets of the bed to account for the increasing influence of friction. In general, $\bar{\bar{S}}_m$ depends on particle properties and local flow conditions including granular temperature Θ_m which is representative of the kinetic energy associated with the fluctuating component of particle velocity. The system of equations is, therefore, closed by considering the transport of Θ_m:

$$\frac{3}{2}\left(\frac{\partial(\varepsilon_m \rho_m \Theta_m)}{\partial t} + \nabla \cdot \left(\varepsilon_m \rho_m \vec{V}_m \Theta_m\right)\right) = \bar{\bar{S}}_m : \nabla \vec{V}_m + \nabla \cdot \vec{q}_{\Theta_m} - \gamma_{\Theta_m} + \phi_{gm} \tag{5}$$

which considers production $\bar{\bar{S}}_m : \nabla \vec{V}_m$, diffusion $\nabla \cdot \vec{q}_{\Theta_m}$ and dissipation through particle-particle γ_{Θ_m} and particle-gas interactions ϕ_{gm}. Finally, $\vec{I}_{gm}$ represents the gas-solids drag force accounting for particle-gas interactions and can be accurately described using the Gidaspow model at low superficial gas velocities ($U/U_{mf} < 4$) [21, 25]. Further details regarding the physical model and governing equations can be found in [13] (and citations therein).

2.2. Boundary Conditions

The wall boundary condition is specified by no-slip for the gas-phase and partial slip for the solids velocity $\vec{V}_{sl}$ computed using the Johnson-Jackson model [26]. This model is based on the simultaneous conservation of solids momentum and granular energy at the walls which are affected by the choice of specularity coefficient ϕ_w representing the loss in particle tangential momentum through friction and collision [19, 21]. Based on detailed comparison of simulations with experimental measurements [21], the present study employs the Li-Benyahia model [27] to determine ϕ_w *in-situ*. Meanwhile, the choice of cylindrical coordinates required boundary conditions at the grid centerline, in addition to the walls, to prevent spurious accumulation of solids. Therefore, radial velocities for both phases at the center are computed using the neighboring flow-field [20]. Finally, uniform gas flow condition is imposed at the inlet even though the effect of perforations is well documented [40, 41]. Therefore, while the methodology described for computing gas flow distribution is invariant to the bed geometry, quantitative predictions close to the distributor may be specific to the simulation setup.

2.3. Numerical Approach

All simulations are performed using MFiX, an open-source code developed at the National Energy Technology Lab (NETL). The governing equations are solved using the SIMPLE (Semi-Implicit Method for Pressure Linked Equations) algorithm wherein the velocity field is first predicted using the pressure field from the previous iteration and subsequently corrected using the continuity (gas-phase) and solids fraction correction equations. Grid cells for all simulations are in the range 8-10 particle diameters to prevent breakdown of continuum assumption of the solids phase [20]. The forward Euler approach is used for time marching with a variable time step to maintain numerical stability; typically in the range 10^{-6} s to 10^{-4} s. More details regarding the numerical algorithm can be found in [28].

3. Fluidization Metrics

At steady state, the gas throughflow Q_{tf} at any axial location can be computed using

$$Q_{tf} = \delta U_{tf} A = UA - (1-\delta) U_d A - Q_b \tag{6}$$

where U is the superficial gas velocity and A is the cross-sectional area of the bed. In terms of the phase volume fractions, $\chi_{tf} = 1 - \chi_d - \chi_b$, where $\chi_d = (1-\delta)U_d/U$ and likewise for the other phases. Quantification of the dense-phase (U_d) and bubbling (δ, Q_b) parameters is described below.

3.1. Dense-Phase Statistics

Dense-phase statistics can be computed by applying suitable filters to simulation data. The bubble void threshold $\varepsilon_{g,b} = 0.7$ so that areas with local void fraction $\varepsilon_g < \varepsilon_{g,b}$ constitute the dense phase and relatively dilute pockets ($\varepsilon_g \geq \varepsilon_{g,b}$) constitute bubbles. Thus, the average void fraction ε_d and gas velocity U_d within the dense-phase can be calculated using

$$\varepsilon_d(y) = \left\langle \frac{\iint \varepsilon_g(x,y,z,t) dA_d}{\iint dA_d} \right\rangle \tag{7}$$

$$U_d(y) = \left\langle \frac{\iint \varepsilon_g(x,y,z,t)\, v_g(x,y,z,t)\, dA_d}{\iint dA_d} \right\rangle \tag{8}$$

where $\langle\ \rangle$ indicates time averaging and dA_d accounts only for areas within the dense phase. Note that the choice of threshold $\varepsilon_{g,b}$ is not trivial because bubble edges are not well-defined discontinuities [17], but is typically in the range 0.7-0.8 (e.g. [29, 30]). In the present study, $\varepsilon_{g,b} = 0.7$ based on previous validation [21], although the statistical description of the dense phase (and other phases as well) is sensitive to the choice of $\varepsilon_{g,b}$. This will be discussed in more detail in Section 4.4.

3.2. Bubble Statistics

The visible bubble flow $Q_b(y)/A$ can be evaluated as $U_b(y)\delta(y)$ where U_b is the time-averaged bubble axial velocity at axial location y and δ denotes the fraction of the cross-sectional area occupied by bubbles i.e.

$$\delta(y) = \left\langle 1 - \frac{1}{A} \iint dA_d \right\rangle \tag{9}$$

Meanwhile, bubble statistics can be quantified using MS3DATA (Multiphase-flow Statistics in 3D using Detection And Tracking Algorithm), which has been developed in-house using MATLAB. While the algorithm is detailed in [22], the overall procedure comprises of the following steps -

- Data Collection - extracting volumetric void fraction data from simulations sampled at 100 Hz for 20s (2000 frames in total)
- Bubble Detection - identifying bubbles using bubble threshold criterion and linking neighboring cells
- Bubble Properties - characterizing bubbles (e.g. location, size, span, shape) by aggregating grid cells forming individual bubbles

Subsequently, bubbles are linked across successive frames and axial velocities are computed using the vertical displacement of bubble centroids in subsequent frames. To prevent erroneous linking arising from high coalescence activity, several filters are imposed and only bubbles with physically feasible linking (based on the data sampling frequency) are considered for averaging. Note that the bubble diameter considered here is based on the bubble volume Ψ_b, i.e. $d_b = \sqrt[3]{6\Psi_b/\pi}$ and volume-averaging (within the discretized section of interest) is used to evaluate time-averaged bubble statistics profiles (for consistency with the calculation of U_d described in Section 3.1). Further details regarding the statistics tool can be found in [22].

4. Results and Discussion

To analyze gas-flow distribution, simulations are conducted for two particles - 1.15 mm LLDPE and 0.5 mm glass particles at U/U_{mf}=2 and 3 in 50 cm diameter fluidized bed. These conditions are chosen to ensure scalability of the hydrodynamics to those seen in commercial systems [13]. Analysis of different phases (dense, visible bubble and throughflow) is presented in detail for the case of LLDPE particles in Sections 4.1-4.4 while the effect of particle properties and scale are examined in Sections 4.5 and 4.6, respectively. A summary of the operating conditions is presented in Table 1, while detailed grid resolution and validation can be found in [13].

Instantaneous visualizations from the simulations using LLDPE particles at U/U_{mf}=3 in a 50 cm diameter bed are presented in Figure 1. Bubbles are formed at the distributor close to the side walls and coalesce laterally towards the bed center as they rise, as also highlighted by the bubble statistics in Figure 2. In a sufficiently deep fluidized bed, bubbles eventually reach the center, rise vertically and form slugs (bubbles comparable to bed dimensions). This transition from bubbling to slugging regimes is consistent across different bed sizes and the corresponding axial height can be characterized by the Froude number based on the bed diameter and excess gas velocity. More detailed description of bubble dynamics and quantitative predictions can be found in [13].

4.1. Dense Phase

The dense-phase constitutes areas of the bed with relatively high solids concentration i.e. the local void fraction $\varepsilon_g < \varepsilon_{g,b}$. Figure 3 shows that the time and cross-section averaged dense phase void fraction ε_d is 1.2-1.3 ε_{mf} close to the distributor, and decreases at higher axial locations, where ε_{mf} is the voidage corresponding to minimum fluidization (estimated as 0.4 using experimentally measured U_{mf} [1]). This is because ε_d increases in areas frequented by bubbles (discussed later in Section 4.3 using Figure 9), which is also the case close to the distributor. Meanwhile, the dense-phase permeability, which is indicative of how easy the fluidizing medium can pass through the bed of solid particles, can be estimated using Ergun's equation [31]:

$$K(\varepsilon_g) = \frac{\varepsilon_g^3 \, d_p^2}{150 \left(1 - \varepsilon_g\right)^2} \tag{10}$$

assuming viscous energy losses to be dominant and perfectly spherical particles. Equation 10 shows that the solids permeability increases in areas with higher void fraction and therefore, the trend in dense-phase gas velocity U_d is similar to that of ε_d. Furthermore, U_d/U_{mf} is relatively insensitive to the superficial gas velocity and the differences between the cases of U/U_{mf}=2 and 3 are only significant close to the distributor. This is because of higher bubble frequency at U/U_{mf}=3. Overall, these observations are consistent with analytical arguments presented by Valenzuela and Glicksman [4], who suggested that the dense phase hydrodynamics must depend only on the average pressure gradient and solids permeability (although the latter is affected by bubbling dynamics, see Section 4.3).

4.2. Visible Bubble Phase

Visible bubble phase refers to gas flow associated with the rising bubbles. As discussed in Section 1, accurate measurements of visible bubble flow Q_b have been challenging because of limitations in diagnostic techniques. On the other hand, numerical simulations provide unrestricted access to the time and spatially resolved field variables and time-averaged Q_b/A can be expressed as δU_b where δ and U_b are the bubble fraction and axial velocity, respectively. δ is quantified from simulation data directly using Equation 9, while U_b is computed from the displacement of centroids of bubbling linked across successive frames [22].

4.2.1. Bubbling Dynamics

Several correlations have been proposed in the literature for bubble rise velocity, both for the case of isolated bubbles and freely bubbling fluidized beds [32]. It is generally accepted that the single bubble rise velocity U_{br} is proportional to the square root of the bubble diameter and the correlation proposed by Davidson and Harrison [33]:

$$U_{br} = 0.71\sqrt{gd_b} \tag{11}$$

continues to be popular. However, extending this correlation to describe dynamics in fluidized beds is challenging because several factors affect bubble rise such as

- bed geometry- bubble flow in rectangular thin lab-scale beds is constrained [11, 12]
- wall resistance- large bubbles and/or those in close proximity to the walls rise slower [1, 34]
- bubble interaction and coalescence- trailing bubbles in near vertical alignment with leading bubbles rise faster [10]
- local solids permeability and velocity [35]

Since these factors are strongly coupled, a broad distribution in bubble velocities is expected. For the present study, this is also highlighted in Figure 4 where the average standard deviation is about 45%. Isolating each of these factors and quantifying their influence on bubble velocities is possible (for instance, the effect of walls is demonstrated in [13]), but quite tedious. Since this study is focused on the average gas distribution in the bed, such detailed description is not pursued and the influence of operating conditions is described using the fitting parameter ϕ:

$$U_{\mathrm{bf}} = \phi\, U_{\mathrm{br}} \tag{12}$$

where ϕ represents the average effect of the aforementioned factors and is listed for all cases in Table 2. For fluidization at low superficial gas velocity ($\mathrm{U/U_{mf}}$=2), ϕ is approximately 1 and increases with superficial gas velocity because of increased bubble interaction and coalescence. Note that a more robust and accurate description of bubble dynamics is only possible if the bubble size and location are accounted for, in addition to the diameter. This is ongoing work and will be presented in future publications.

Figure 4 also compares average bubble axial velocities with the correlation proposed by Hilligardt and Werther [9] using their measurements in large beds:

$$U_{HW} = \psi(U - U_{\mathrm{mf}}) + \theta U_{br} \tag{13}$$

$$\psi = \begin{cases} 0.67 \\ 0.28^{*} \end{cases} \qquad \theta = \begin{cases} 2\sqrt{D} & \text{Geldart B} \\ 0.87 & \text{Geldart D} \end{cases}$$

* average between $y/D \in [0, 1]$

Bubble axial velocity predictions, based on regression (Equation 12), lie within the Hilligardt-Werther correlations for Geldart B ($U_{\mathrm{HW,B}}$) and D ($U_{\mathrm{HW,D}}$) particle-types. This is reasonable considering that although classified as Geldart B, particles considered in this study may exhibit bubbling characteristics of Geldart D group [9]. Nevertheless, Figure 4 highlights the sensitivity of bubble correlations to particle properties, in addition to superficial gas velocity and bed geometry [32]. Since this study is focused on developing a framework for quantifying gas-distribution, visible bubble flow is, hereafter, estimated using simulation data directly and bubble correlations proposed in literature are neither verified nor ranked regarding their accuracy or applicability.

Figure 5 compares the correlation of bubble diameter-axial velocity predicted using different sampling frequencies 25, 50 and 100 Hz. In general, the average description of bubbling dynamics (i.e. coefficient ϕ in

Equation 12) is relatively insensitive to the frequency of volumetric data acquisition. However, the number of reliable links decreases significantly as the time-resolution of data is decreased, visually evident by the number density of links when the sampling frequency is decreased from 100 Hz in Figure 4 (2000 frames considered for 20s) to 50 Hz in Figure 5 (1000 frames considered for 20s). This is because of difficulties posed by high bubble activity (coalescence and splitting) at relatively high superficial gas velocities ($U/U_{mf} > 1.5$). Thus, despite the high computational cost of processing large volumes of data, all cases in this study are analyzed by sampling data at 100Hz.

4.2.2. Visible Bubble Flow Statistics

Bubbling fluidization of Geldart B particles in large beds is characterized by the formation of small bubbles close to the side walls, near the distributor, that rise laterally towards the bed centerline [13, 35]. This feature can be clearly observed in Figure 2a through the bubble centroid map. Note that in this case, the bed is sufficiently deep (initial height = 50 cm) so that most bubbles are able to reach the bed centerline before erupting into the freeboard. Further, as bubbles rise, they interact and coalesce forming larger ones (and slugs, typically in lab-scale beds), as depicted in Figure 2b. Finally, Figure 2c quantifies the radial distribution of gas flow through bubbles, at different axial locations- 5, 15, 30 and 45 cm from the distributor. The peak in gas flow corresponds to the radial location most frequented by bubbles, and this peak shifts towards the centerline with increasing axial distance from the distributor, consistent with observations in Figures 2a and 2b. The overall gas flow within bubbles (including both visible bubble flow and throughflow), which is represented by the area under the curve in Figure 2c, also increases upwards, from 40% of the total gas flow at y=0.05 m to almost 68% at y=0.45 m. This is because of the formation of large bubbles as well as rise in gas throughflow higher up in the bed (discussed later in Section 4.3).

Cross-section averaged statistics for the bubble phase are presented in Figure 6, for the fluidization of LLDPE particles at U/U_{mf}=2 and 3. Close to the distributor, interstitial gas through the dense phase U_i ($=U_g/\varepsilon_g$) is faster than the rise of small bubbles, and contributes to the increase in bubble size (and hence, δ). As bubbles coalesce and grow, U_b increases (proportional to $\sqrt{d_b}$) and the contribution of interstitial flow decreases so that δ is relatively unchanged through the bed interior. Note that there is slight decrease in δ close to the freeboard section; this is due to the formation of elongated bubbles (the average aspect ratio of bubbles increases steadily from 0.5 at the distributor to almost 1.2 at y = 50 cm, see [13] for more details). Similar arguments can be used to explain the impact of higher superficial gas velocity; in this case δ increases 1.5× when U/U_{mf} is increased from 2 to 3, and larger bubbles also rise faster (the coefficient ϕ increases, see Table 2). Overall, Figure 6 shows that the mass fraction of the gas-flow in the visible bubble phase ($\chi_b = \delta U_b/U$) is about 20%, which is considerably higher than estimates by Glicksman and McAndrews [12] based on their experiments in larger-scale beds. The key difference is that they considered low-velocity fluidization ($U/U_{mf} \leq 1.8$) in wide rectangular beds where (a) preferential bubble pathways were not observed, unlike in cylindrical beds where gas-flow at the distributor is skewed towards the bed walls [13] and (b) the average bubble fraction is low $\delta \in [0.05 - 0.10]$, both factors contributing to reduced bubble interaction and coalescence.

4.3. Throughflow

Gas-throughflow is commonly observed in the fluidization of large particles where bubbles are typically slow and interstitial gas (in the dense phase) may enter the base of the bubbles and exit through the top, as is schematically shown in Figure 7 for a typical bubble observed in the fluidization of LLDPE particles at U/U_{mf}=3. Thus, there is considerable gas-exchange between the dense and bubble phases, although in the presence of bubble swarms (Figure 8), low resistance pathways are created for convenient shortcut of gas through the bed and contact with the dense-phase is minimal. This phenomenon adversely affects gas residence times, and consequently solids mixing, and is not desirable for fluidized bed operation. Note that this is unlike the case of bubbling fluidization of fine (Geldart A) particles where bubbles rise significantly faster and exiting gas gets recirculated towards the bubble base [1].

Several studies have attempted to quantify throughflow using detailed bubble statistics obtained from high-resolution experimental visualizations and numerical studies (e.g. [17, 18]). While useful for analyzing throughflow fundamentally, conclusions and correlations from these studies are limited because bubble dynamics in larger beds significantly differ from the case of thin-rectangular beds [21]. In larger beds, 3D calculations are expensive [22] and generalized description of throughflow may not be possible because of significantly higher bubble interaction and coalescence (as compared to 2D flows). Therefore, throughflow statistics are quantified using the steady-state gas-flow balance $\chi_{tf} = 1 - \chi_d - \chi_b$, while trends are explained qualitatively using detailed flow-field calculations.

Figures 9 and 10 quantify the void fraction and gas axial velocity field, respectively, in and around bubbles for the fluidization of LLDPE particles at U/U_{mf}=3. These calculations are performed accurately by coupling the bubble detection tool (MS3DATA) with the flow-field as follows: the bubble detection tool [22] identifies any bubble b_i as a collection of linked (neighboring) grid cells, each of which satisfies the threshold criterion $\varepsilon_g \geq \varepsilon_{g,b}$. Consequently, the bubble contour Ω_i is identified as the subset of these cells (with cell centers $\mathbf{x}_{\Omega_i}$) in contact with the dense-phase so that the distance of cells $\mathbf{x}_{ij}$, interior or exterior to the bubbles, is computed using

$$r_j = \min_{\Omega_i} |\mathbf{x}_{ij} - \mathbf{x}_{\Omega_i}| \tag{14}$$

Grid cells in and around bubbles can, therefore, be segregated based on their distance from the bubble boundary and statistical data from about 100 bubbles of different sizes and spatial locations identified in 15 randomly selected time instants is presented in Figures 9 and 10. Note that these calculations are based on the simulation grid resolution $\sim$ 7 mm for LLDPE particles and make no assumptions regarding the bubble shape or any other characteristics. Figure 9 shows that ε_g around bubbles decays exponentially with distance r from bubble boundary but is considerably higher than ε_{mf} upto r=4 cm. Note that r has not been normalized by the bubble radius because most bubbles are deformed; typical aspect ratios are in the range 0.2-1.5 (see Figure 11). Nevertheless, it follows that the dense phase voidage is higher in areas frequented by bubbles, which is the case close to the distributor and can also be observed in Figure 3. Meanwhile, since solids permeability increases at higher ε_g (Equation 10), it follows that the gas axial velocity v_g in the vicinity of bubbles must also be higher than U_{mf}, which is indeed the case as presented in Figure 10. Further, it is interesting to note that even in areas with similar ε_g, gas flow is significantly higher in the vicinity of bubbles ($r < 4$ cm). This suggests that the solids permeability (Equation 10) also depends on the presence of bubbles, in addition to the local void fraction, and is one of the limitations of potential-flow theory based models proposed in literature.

In a similar way, the flow-field within bubbles is investigated and presented in Figure 11. In every bubble, average throughflow velocity is computed based on the gas flow relative to the bubble, whose rise velocity is predicted using the linking algorithm described in Section 3.2. Figure 11 shows significant throughflow for smaller bubbles ($U_{tf}/U_b \in [1.5, 3.0]$), as compared to the larger ones which rise much faster ($U_b \propto \sqrt{d_b}$). This trend is qualitatively consistent with calculations based on 2D simulations in [18]. On the other hand, throughflow increases with bubble aspect ratio AR; for elongated bubbles, the ratio $U_{tf}/U_b \in [2.0, 3.0]$. This dependence on AR is consistent with predictions by Valenzuela and Glicksman [4], although their analytical model underpredicts throughflow because it assumes (a) bubbles in isolation and (b) constant U_d. As demonstrated in Figures 9 and 10, these assumptions are invalid in the vicinity of bubble chains (or swarms) where both the local solids permeability and the dense-phase gas velocity are significantly higher.

Based on the detailed analysis presented above, it is clear that throughflow is affected by the local dense-phase conditions and bubble characteristics. This can be observed in Figure 12 as χ_{tf} grows significantly with vertical distance from the distributor. The rate of growth, however, falls beyond y=10 cm because (a) larger bubbles rise faster and (b) bubble frequency is reduced, resulting in lower permeability of the dense phase. Similar arguments can be used to explain the increase in χ_{tf}, from approximately 25% to 40% when the superficial gas velocity is raised from $2U_{mf}$ to $3U_{mf}$. This analysis reinforces the need for good distributor designs to control bubbling dynamics and suggests gas injection through multiple inlets because increasing the superficial gas flow through the distributor does not contribute to better gas and solids mixing. Overall, it is clear that trends in throughflow can be described by analyzing the bubble size and spatial distribution. A more fundamental understanding will require further simulations and detailed analysis, and will be discussed in future publications.

4.4. Gas Flow Distribution

The residence time distribution of gas-flow can be calculated by integrating the inverse of the phase-velocities:

$$\tau_d = \int \frac{\varepsilon_d(y)}{U_d(y)} dy \quad \tau_b = \int \frac{1}{U_b(y)} dy \quad \tau_{tf} = \int \frac{\varepsilon_b(y)}{U_{tf}(y)} dy \tag{15}$$

where ε_b denotes the average void fraction within bubbles, and is computed in a way similar to ε_d using Equation 7. Based on the voidage distribution presented in Figure 9, it is evident that ε_b increases with bubble size and is typically in the range 0.85-0.95. Gas residence time distribution for the fluidization of LLDPE particles is presented in Figure 13. All time estimates are normalized with respect to $\tau_0 = H_0\varepsilon_0/U$, which corresponds to the case of uniform gas flow through the bed. The overall inhomogeneity in bed mixing can, therefore, be

characterized by (a) the throughflow composition χ_{tf} and (b) the disparity in time-scales between the dense phase and throughflow phase τ_d/τ_{tf}.

Figure 13 shows that for U/U_{mf}=2, χ_d=58% and the bubble and throughflow phases constitute 19% and 23%, respectively. Comparison of time-estimates shows that the dense and bubble phases have similar residence times in the bed ($\tau_d/\tau_0 = 1.28$ and $\tau_b/\tau_0 = 1.16$), while the throughflow is about 1.7× faster. As the superficial gas velocity is raised to $3U_{mf}$, (a) χ_d decreases by almost 20% with majority of the excess gas contributing to higher throughflow (χ_{tf} increases from 23% to 38%) and (b) the ratio τ_d/τ_{tf} grows to approximately 2.5. Both observations suggest that raising U/U_{mf} for large particles increases the fraction of additional gas that constitutes throughflow. Note that the exchange of gases between phases is implicit to residence-time calculations; for instance, mass transfer from the dense-phase to bubbles (decreasing χ_d as shown in Figure 3) contributes to their growth and acceleration resulting in shorter residence of gas within bubbles (τ_b and τ_{tf}). In reality, the residence time of injected tracer gas is expected to be in the range $[\tau_{tf}, \tau_d]$ and is dependent on the bubble frequency and coalescence rate.

Note that gas-distribution and residence time statistics (from both experiments and simulations) are sensitive to the choice of void threshold $\varepsilon_{g,b}$, because bubble edges are not well-defined discontinuities (Figure 9). The sensitivity further increases with superficial gas velocity and can be explained using Figure 14 indicating the distribution and momentum of gas flow in terms of the local void fraction, for the fluidization of LLDPE particles at U/U_{mf}=2 and 3. For both cases, most (60-70%) of the bed volume is minimally fluidized ($\varepsilon_{mf} \approx 0.4$), but as U/U_{mf} is raised to 3, (a) fraction of the bed occupied by relatively dilute pockets ($\varepsilon_g \in [0.6, 1.0]$) increases 2× and (b) most of the additional gas supplied contributes towards higher gas flow in these areas. For fluidization at U/U_{mf}=3, the sensitivity of gas-distribution and residence time statistics to the choice of $\varepsilon_{g,b}$ is presented in Figure 15. With $\varepsilon_{g,b} = 0.8$, χ_d increases from 0.38 to 0.46 (about 20%) while τ_d decreases by 8% because of higher solids permeability within the dense-phase (average ε_d increases). On the other hand, χ_b reduces by about 20%, although the change in τ_b is minimal because the volume averaged bubble velocity is significantly dependent on the larger (>4 cm) bubbles, whose sizes are relatively unaffected by the choice of $\varepsilon_{g,b}$. Overall, caution must be exercised while computing phase-specific statistics and validating with experimental measurements, especially for bubbling fluidization at relatively high velocities ($U/U_{mf} \geq 3$). For the present study, $\varepsilon_{g,b}$ is set at 0.7 based on previous validation and analysis [21].

4.5. Effect of Particle Properties

The methodology described in Sections 4.1-4.4 is repeated for the fluidization of glass particles (0.5 mm, 2500 kg/m^3) at U/U_{mf}=2 and 3 in a 50 cm diameter bed. Simulation data is analyzed and phase-specific calculations are performed, similar to the case of LLDPE particles, but not presented in detail for brevity. Instead, overall statistics for gas residence-time and phase distribution are presented in Figure 16. At low superficial gas velocity, bubbles are small and majority of the gas flow is found in the dense phase (χ_d=55%). Two-thirds of the remaining gas-flow constitutes throughflow, the residence time of which is about 2× shorter. As U/U_{mf} is increased to 3, local dense-phase conditions are relatively unaffected ($U_d/U_{mf} \approx 1$), although χ_d decreases from 55% to 34%. Most of this deficit contributes to more visible bubble flow (from 15% at U/U_{mf}=2 to 30% at U/U_{mf}=3), which is unlike the case of LLDPE particles where substantial increase in throughflow is observed. This trend of lower gas-bypass in the fluidization of smaller particles is consistent with experimental findings [6] and may be related to the lower solids permeability (Equation 10).

It is interesting to compare the predictions of LLDPE particles at U/U_{mf}=2 (Figure 13a) with glass particles at U/U_{mf}=3 (Figure 16b), since the superficial gas velocities for these cases are similar (48 cm/s for LLDPE and 54 cm/s for glass). For the former case, (a) χ_d is significantly higher (58% as compared to 34% for glass particles) and (b) residence time-scales are less disparate (τ_d/τ_{tf}=1.7 as compared to 2.3 for glass particles). Both observations can be explained qualitatively by analyzing bubble dynamics: for similar superficial gas velocities, the excess gas (=$U-U_{mf}$) for smaller particles is higher so that larger bubbles are formed (and/or at higher frequency), which also rise faster through the bed [4, 6].

4.6. Effect of Bed Diameter

Finally, the effect of size is analyzed by comparing the gas-flow distribution for the fluidization of LLDPE particles at U/U_{mf}=3 in different diameter (15-70 cm) fluidized beds. Typical instantaneous visualizations, presented in Figure 17 for all cases, clearly demonstrate the difference in bubbling dynamics between cases: accelerated coalescence and growth in smaller beds (15 and 30 cm diameter) because wall confinement results in larger bubbles. This observation is presented quantitatively in Figure 18 which shows that both δ and bubble diameter d_b decrease with increasing bed size. Note that, it was demonstrated in [13] that the dynamics in

the 50 cm and 70 cm diameter beds are similar and therefore, are likely to be scalable. Detailed phase-specific statistics are presented in Figure 19. As the bed diameter is increased, χ_b decreases by almost 20% because of relatively small bubbles (consistent with Figure 18), although the trend in τ_b is not monotonic. This is because although bubbles become smaller, similar-sized bubbles rise faster in larger beds (i.e. ϕ in Equation 12 increases). The minimum τ_b for the 30 cm diameter bed is observed for all cases (LLDPE and sand particles at U/U_{mf}=2 and 3), but could be specific to the range of operating conditions analyzed here. Nevertheless, smaller bubbles at wider beds also explain the increase in χ_d (20% in 15 cm to 38% in 50 cm diameter bed) while τ_d decreases because of lower wall resistance. Interestingly, gas flow constituting throughflow remains relatively constant $\sim$ 40% across bed scale; high throughflow results from elongated bubbles in smaller beds (Figure 11), and formation of bubble chains in larger beds [12, 35]. Overall, the methodology developed in this study can be employed to analyze gas distribution in fuel conversion systems and predict the performance of scaled-up reactors. Hydrodynamic simulations presented here indicate higher gas-flow in the dense-phase which suggests faster solids axial mixing in larger beds.

5. Conclusion

Gas flow distribution affects gas residence time and solids mixing, both of which are critical to the performance of fluidized beds. Recognizing this, substantial modeling and experimental effort has been invested in the past towards describing gas flow reliably, although limited by capabilities of diagnostic equipment especially under the harsh conditions most beds operate in. This study is, therefore, focused on the development of a rigorous computational framework to describe gas flow distribution accurately using data from fine-grid CFD simulations. The methodology is presented in detail for the fluidization of LLDPE particles (1.15 mm, 800 kg/m^3) in a 50 cm diameter bed (initial height 50 cm), because hydrodynamics in this bed have been shown to become relatively independent of the bed diameter [13], while the effects of particle properties and bed diameter are also investigated.

The total gas-flow in bubbling fluidized beds can be divided into: (a) dense-phase in areas of relatively high solids concentration (b) visible bubble-phase associated with rising bubbles and (c) throughflow-phase which mostly bypasses through bubbles. Irrespective of the operating parameters (particle properties and superficial gas velocity), the dense-phase conditions can be approximated as being minimally fluidized, except in the vicinity of bubbles where the local voidage and gas velocity depend on the distance from bubble boundaries. On the other hand, bubbling dynamics are dependent on the excess gas velocity (=U-U_{mf}); increasing the superficial flow leads to the formation of larger bubbles (and slugs) through accelerated interaction and coalescence. Finally, throughflow may be correlated with the solids permeability in the vicinity of bubbles; areas frequented by bubbles have higher dense-phase voidage offering low resistance for interstitial gas to escape through bubbles. This is particularly the case close to the distributor where (a) bubbles are small and their rise very slow ($U_b \propto \sqrt{d_b}$) and (b) preferential bubble pathways are observed, especially in larger beds.

The methodology developed is subsequently applied to investigate the impact of operating conditions and reactor scale. Generally speaking, as the superficial velocity is increased, gas flow within the bubble and throughflow phases increases at the expense of dense-phase flow. However, distinct differences are observed in the fluidization of smaller glass particles (0.50 mm, 2500 kg/m^3): when U/U_{mf} is raised from 2 to 3, visible bubble flow increases by 15%, unlike the case of LLDPE particles where substantial increase in throughflow is observed. This growth in the visible bubble flow in the case of smaller particles is consistent with experimental measurements reported in the literature and may be related to the higher solids permeability. Thus, increasing U/U_{mf} adversely affects fluidized bed operation, especially in the case of large particles, because a substantial fraction of the added gas flow short circuits through bubbles with 2$\times$ shorter residence time and contributes minimally to solids mixing. Finally, analysis in different bed sizes shows that as the bed diameter is increased (from 15 to 70 cm), (a) bubbles are relatively small, but similar sized bubbles rise faster, and (b) the dense-phase flow increases, both factors contributing to faster solids (axial) mixing. Interestingly, throughflow constitutes $\sim$ 40% of the total gas-flow and remains uniform across scales. Significant throughflow is not surprising because of elongated bubbles in lab-scale beds and the formation of bubble chains in larger beds. Insights from this study and the developed methodology can be used for investigating gas flow and developing reduced order models for the hydrodynamics in complex fuel conversion systems.

6. Acknowledgment

The authors gratefully acknowledge BP for funding this research. This research was supported in part by an appointment to the National Energy Technology Laboratory Research Participation Program, sponsored by

the U.S. Department of Energy and administered by the Oak Ridge Institute for Science and Education.

References

[1] D. Kunii and O. Levenspiel. *Fluidization Engineering*. 1991.

[2] J.R. Grace and D. Harrison. The behavior of freely bubbling fluidized beds. *Chemical Engineering Science*, 24:497–508, 1969.

[3] C. Yacono, P. N. Rowe, and H. Angelino. An analysis of the distribution of flow between phases n a gas fluidized bed. *Chemical Engineering Science*, 34:789–800, 1979.

[4] J.A. Valenzuela and L.R. Glicksman. Gas flow distribution in a bubbling fluidized bed. *Powder Technology*, 44(2):103 – 113, 1985.

[5] L. Jones and L.R. Glicksman. An experimental investigation of gas flow in a scale model of a fluidized-bed combustor. *Powder Technology*, 45(3):201 – 213, 1986.

[6] J. Baeyens and S.Y. Wu. Bed expansion and the visible bubble flow rate in gas fluidized beds. *Advanced Powder Technology*, 3(3):163 – 189, 1992.

[7] R.D. Toomey and H.F. Johnstone. Gaseous fluidization of solid particles. *Chemical Engineering Progress*, 48:220–226, 1952.

[8] W. K. Lord. *Bubbly flow in Fluidized beds of large particles*. PhD thesis, Massachusetts Institute of Technology, 1983.

[9] K. Hilligardt and J. Werther. Local bubble gas holdup and expansion of gas/solid fluidized beds. *German Chemical Engineering*, 9:215–221, 1986.

[10] L.R. Glicksman, W.K. Lord, and M. Sakagami. Bubble properties in large-particle fluidized beds. *Chemical Engineering Science*, 42(3):479 – 491, 1987.

[11] D. Geldart. The size and frequency of bubbles in two- and three-dimensional gas-fluidised beds. *Powder Technology*, 4(1):41 – 55, 1970.

[12] L.R. Glicksman and G. McAndrews. The effect of bed width on the hydrodynamics of large particle fluidized beds. *Powder Technology*, 42(2):159 – 167, 1985.

[13] A. Bakshi, C. Altantzis, R.B. Bates, and A.F. Ghoniem. Study of the effect of reactor scale on fluidization hydrodynamics using fine-grid CFD simulations based on the two-fluid model. *Powder Technology*, 299:185 – 198, 2016.

[14] J.F. Davidson, R. Clift, and D. Harrison. *Fluidization. Second Edition*. Academic Press, 1985.

[15] M. Gautam, J.T. Jurewicz, and S.R. Kale. An experimental investigation of throughflow velocities in two-dimensional fluidized bed bubbles: Laser doppler anemometer measurements. *Journal of Fluids Engineering*, 116:605–612, 1994.

[16] J.R. Grace and R. Clift. On the two-phase theory of fluidization. *Chemical Engineering Science*, 29(2):327 – 334, 1974.

[17] J.A. Almendros-Ibanez, D. Pallares, F. Johnsson, and D. Santana. Voidage distribution around bubbles in a fluidized bed: Influence on throughflow. *Powder Technology*, 197(12):73 – 82, 2010.

[18] F. Hernndez-Jimnez, A. Gmez-Garca, D. Santana, and A. Acosta-Iborra. Gas interchange between bubble and emulsion phases in a 2d fluidized bed as revealed by two-fluid model simulations. *Chemical Engineering Journal*, 215216:479 – 490, 2013.

[19] C. Altantzis, R.B. Bates, and A.F. Ghoniem. 3D Eulerian modeling of thin rectangular gas-solid fluidized beds: Estimation of the specularity coefficient and its effects on bubbling dynamics and circulation times. *Powder Technology*, 270, Part A(0):256 – 270, 2015.

[20] A. Bakshi, C. Altantzis, and A.F. Ghoniem. Towards accurate three-dimensional simulation of dense multi-phase flows using cylindrical coordinates. *Powder Technology*, 264(0):242 – 255, 2014.

[21] A. Bakshi, C. Altantzis, R.B. Bates, and A.F. Ghoniem. Eulerian-Eulerian simulation of dense solidgas cylindrical fluidized beds: Impact of wall boundary condition and drag model on fluidization. *Powder Technology*, 277(0):47 – 62, 2015.

[22] A. Bakshi, C. Altantzis, R.B. Bates, and A.F. Ghoniem. Multiphase-flow statistics using 3d detection and tracking algorithm (ms3data): Methodology and application to large-scale fluidized beds. *Chemical Engineering Journal*, 293:355 – 364, 2016.

[23] M. Syamlal, W. Rogers, and T. J. O'Brien. *MFIX Documentation Theory Guide*, 1993.

[24] D.G. Schaeffer. Instability in the evolution equations describing incompressible granular flow. *Journal of Differential Equations*, 66:19–50, 1987.

[25] D. Gidaspow. *Multiphase Flow and Fluidization: Continuum and Kinetic Theory Descriptions*. Boston: Academic, 1994.

[26] P.C. Johnson and R. Jackson. Frictional-collisional constitutive relations for granular materials, with application to plane shearing. *J. Fluid Mech.*, 176:67–93, 1987.

[27] T. Li and S. Benyahia. Revisiting johnson and jackson boundary conditions for granular flows. *AIChE Journal*, 58(7):2058–2068, 2012.

[28] M. Syamlal. *MFIX Documentation Numerical Technique*, January 1998.

[29] V. Verma, J. T. Padding, N. G. Deen, J. A. M. (Hans) Kuipers, F. Barthel, M. Bieberle, M. Wagner, and U. Hampel. Bubble dynamics in a 3-d gassolid fluidized bed using ultrafast electron beam x-ray tomography and two-fluid model. *AIChE Journal*, 60(5):1632–1644, 2014.

[30] A. Busciglio, G. Vella, G. Micale, and L. Rizzuti. Analysis of the bubbling behaviour of 2d gas solid fluidized beds: Part i. digital image analysis technique. *Chemical Engineering Journal*, 140(13):398 – 413, 2008.

[31] S. Ergun. Fluid flow through packed columns. *Chemical Engineering Progress*, 48:89–94, 1952.

[32] S. Karimipour and T. Pugsley. A critical evaluation of literature correlations for predicting bubble size and velocity in gassolid fluidized beds. *Powder Technology*, 205(13):1 – 14, 2011.

[33] J.F. Davidson and D. Harrison. *Fluidized Particles*. Cambridge University Press, 1963.

[34] G. Dons, L. Massimilla, S. Crescitelli, and G. Volpicelli. Solid flow pattern at the wall of a fluidization column induced by single bubbles. *Powder Technology*, 6(4):217 – 224, 1972.

[35] J. Werther. Influence of the bed diameter on the hydrodynamics of gas-fluidized beds. *AIChE Symp. Series*, 70(141):53–64, 1974.

[36] M.A. van der Hoef, M. van S. Annaland, N.G. Deen, and J.A.M. Kuipers. Numerical Simulation of Dense-Gas-Solid Fluidized Beds: A Multiscale Modeling Strategy. *Annual Rev. Fluid Mech.*, 40:47–70, 2008.

[37] P.N. Rowe, B.A. Partiridge, A.G. Cheney, G.A. Henwood, and E. Lyall. The mechanisms of solid mixing in fluidized beds. *Transactions of the Institute of Chemical Engineers*, 43:271–286, 1965.

[38] J. Werther. Convective solids transport in large diameter gas fluidized beds. *Powder Technology*, 15(2):155–167, 1976.

[39] M. Stein, Y.L. Ding, J.P.K. Seville, and D.J. Parker. Solids motion in bubbling gas fluidized beds. *Chemical Engineering Science*, 55(22):5291–5300, 2000.

[40] S. Mori and C. Y. Wen Estimation of Bubble Diameter in Gaseous Fluidized Beds. *AIChE Journal*, 21(1):109–115, 1975.

[41] A.C. Rees, J.F. Davidson, J.S. Dennis, P. S Fennell, L.F. Gladden, A.N. Hayhurst, M.D. Mantle, C.R. Muller, and A.J. Sederman The nature of the flow just above the perforated plate distributor of a gas-fluidised bed, as imaged using magnetic resonance. *Chemical Engineering Science*, 61:6002–6015, 2006.

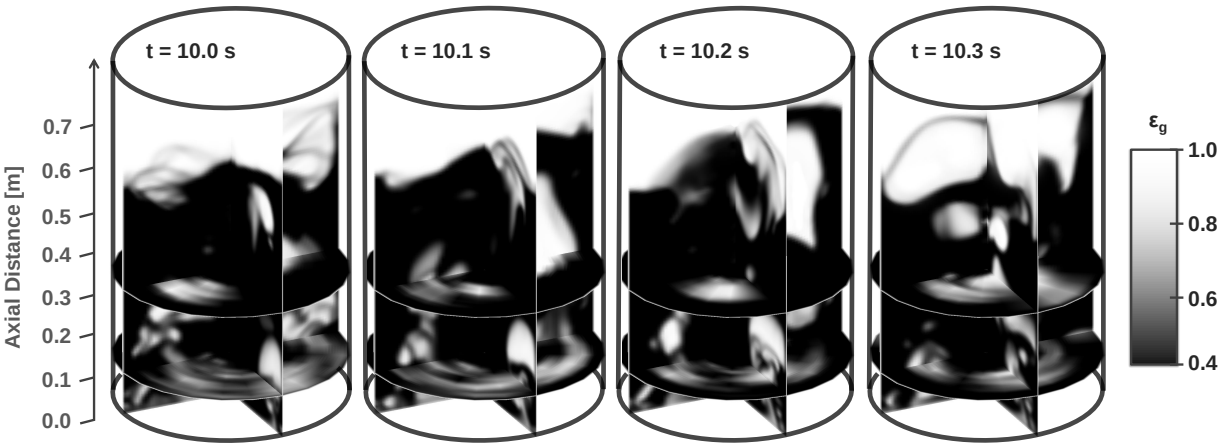

Figure 1: Instantaneous visualizations of fluidization of LLDPE particles at U/U_{mf}=3 in 50 cm diameter bed (H_0 = 50 cm).

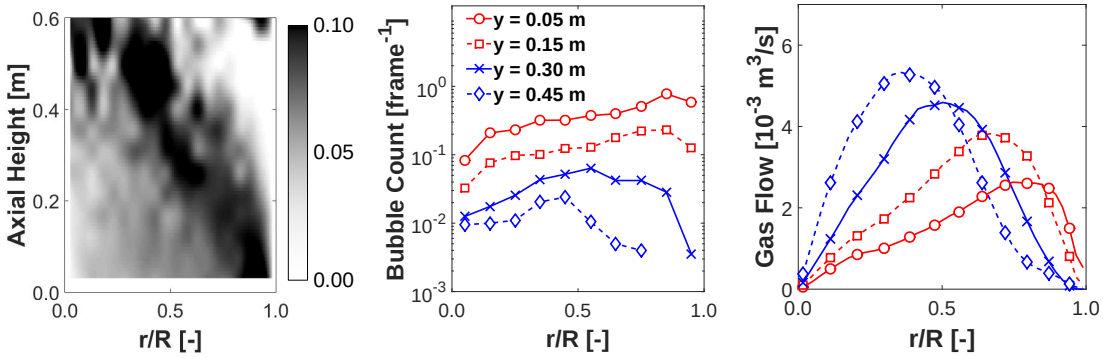

(a) Bubble Centroid Map (b) Bubble Count (c) Bubble Gas Flow

Figure 2: Time-averaged bubble statistics for fluidization of LLDPE particles at U/U_{mf}=3 in 50 cm diameter bed (H_0 = 50 cm). Bubble flow is characterized using (a) centroid map highlighting bubble pathways (gray scale indicates frequency), (b) radial distribution of bubble frequency and (c) gas flow through bubbles at axial locations y=0.05-0.45 m.

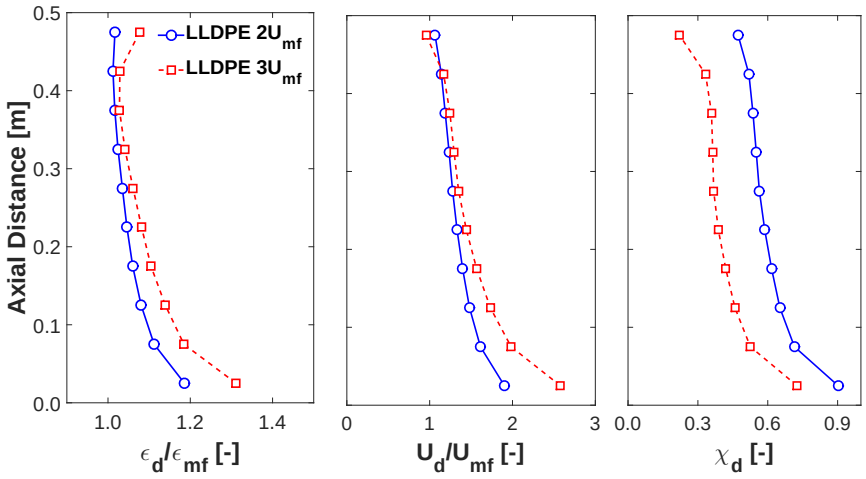

Figure 3: Time and cross-section averaged dense phase statistics for fluidization of LLDPE particles at U/U_{mf}=2 and 3 in 50 cm diameter bed (H_0 = 50 cm)

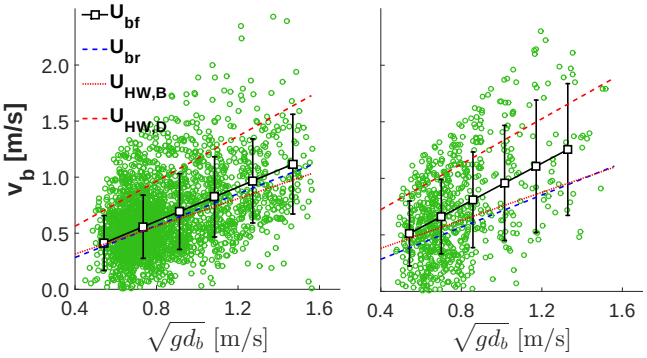

(a) LLDPE, U/U_{mf}=2 (b) LLDPE, U/U_{mf}=3

Figure 4: Linked bubble velocity and diameter for fluidization of LLDPE particles at U/U_{mf}=2 and 3 in 50 cm diameter bed (H_0 = 50 cm). U_{bf} is the regressed fitting (Equation 12) with coefficient ϕ listed in Table 2. U_{br} is the single bubble rise velocity described by Equation 11. U_{HW} is the correlation proposed by Hilligardt and Werther [9] (Equation 13) and subscripts B and D denote Geldart B and D particles, respectively.

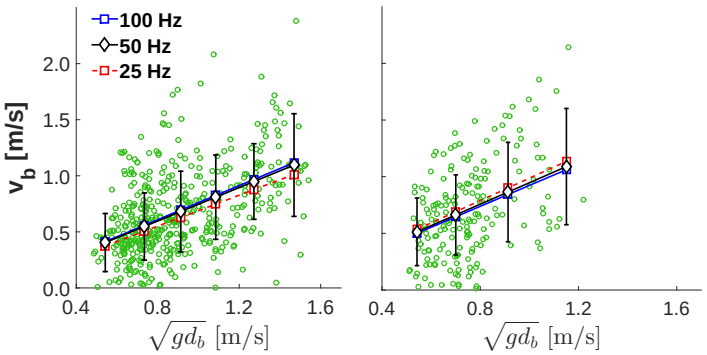

(a) LLDPE, U/U_{mf}=2 (b) LLDPE, U/U_{mf}=3

Figure 5: Linked bubble velocity and diameter for fluidization of LLDPE particles at U/U_{mf}=2 and 3 in 50 cm diameter bed (H_0 = 50 cm), and its dependence on data sampling frequency (25, 50 and 100 Hz). Green circular markers indicate reliably linked instances at 50 Hz sampling and best fit equation is obtained using linear regression (Equation 12)

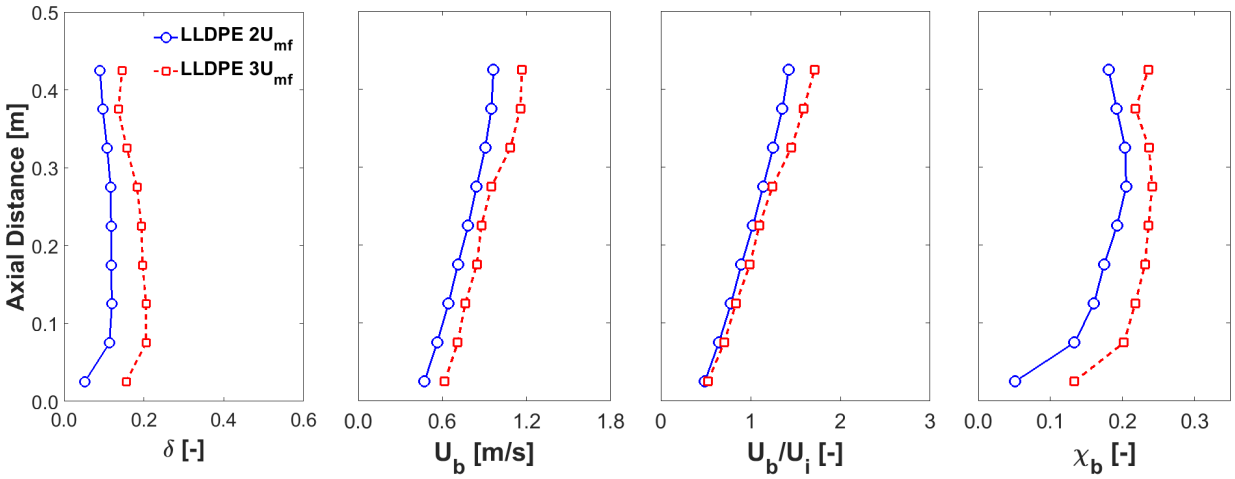

Figure 6: Time and cross-section averaged bubble phase statistics for fluidization of LLDPE particles in 50 cm diameter bed (H_0 = 50 cm)

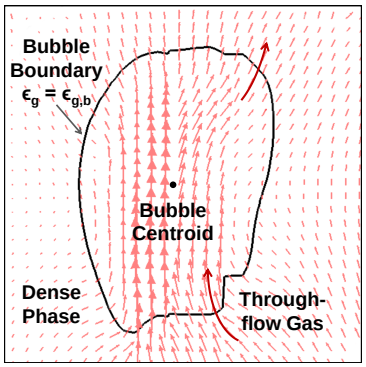

Figure 7: Gas velocity field (red vectors) with respect to a typical rising bubble (black colored contour) obtained from fluidization simulations of LLDPE particles at U/U_{mf}=3

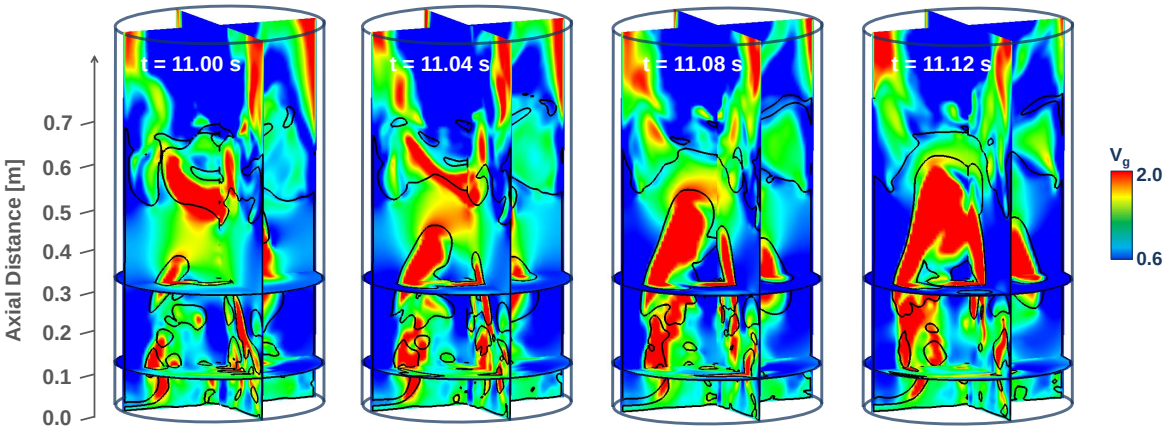

Figure 8: Instantaneous visualizations of bubbles (black colored contours) overlayed with the gas axial velocity field for fluidization of LLDPE particles at U/U_{mf}=3.

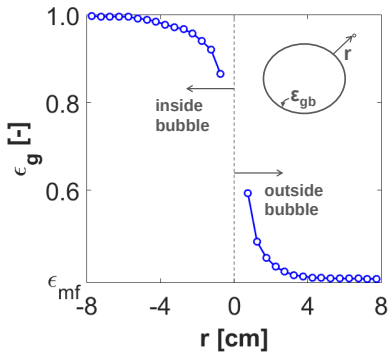

Figure 9: Voidage distribution in and around bubbles for the fluidization of LLDPE particles at U/U_{mf}=3. Statistics are computed using spatially-resolved void fraction data at 15 randomly-selected time-instants (considering about 100 bubbles in the bed interiors). r is the distance from bubble boundary calculated using Equation 14 and the void threshold for bubble detection $\varepsilon_{g,b}$=0.7.

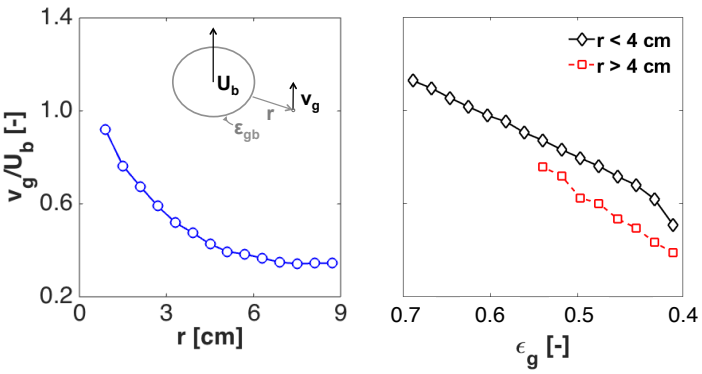

Figure 10: Gas velocity distribution around bubbles (normalized by the bubble axial velocity U_b) for the fluidization of LLDPE particles at U/U_{mf}=3. Statistics are computed using spatially-resolved void fraction data at 15 randomly-selected time-instants (considering about 100 bubbles in the bed interiors). r is the distance from bubble boundary calculated using Equation 14 and the void threshold for bubble detection $\varepsilon_{g,b}$=0.7.

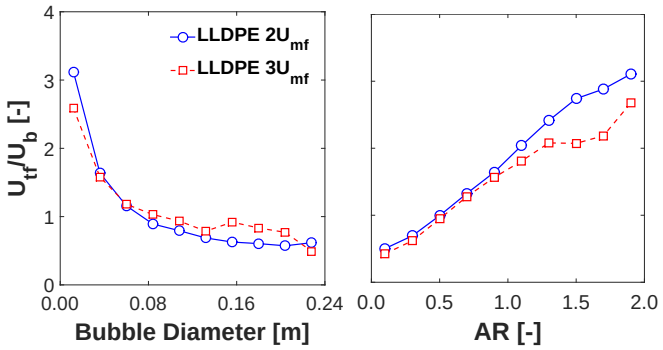

Figure 11: Ratio of throughflow velocity to bubble axial velocity in terms of bubble diameter and aspect ratio for fluidization of LLDPE particles at U/U_{mf}=2 and 3 in 50 cm diameter bed (H_0 = 50 cm)

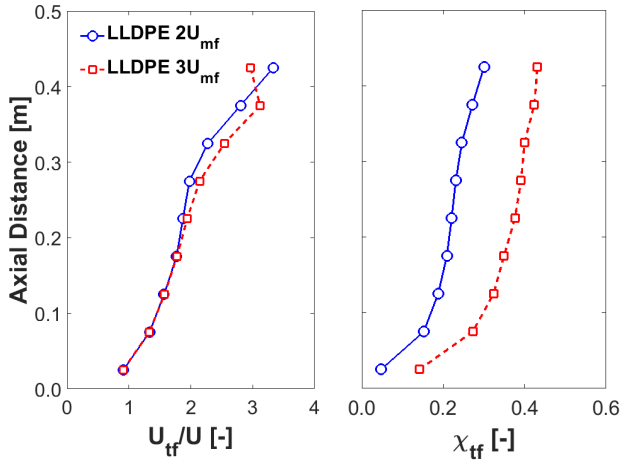

Figure 12: Time-averaged throughflow phase statistics for fluidization of LLDPE particles at U/U_{mf}=2 and 3 in 50 cm diameter bed (H_0 = 50 cm)

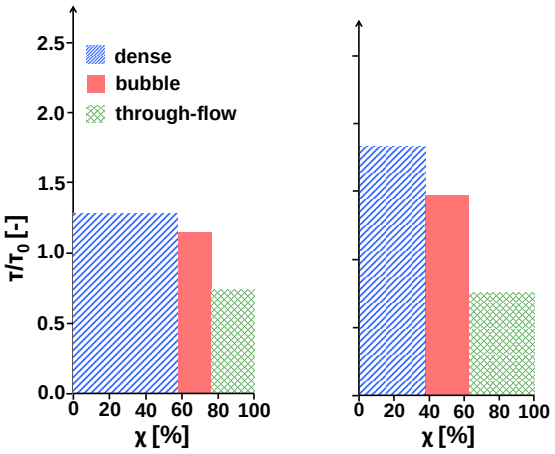

(a) LLDPE $2U_{mf}$ (b) LLDPE $3U_{mf}$

Figure 13: Residence time distribution of gas flow for fluidization of LLDPE particles at U/U_{mf}=2 and 3 in 50 cm diameter bed (H_0 = 50 cm). All estimates are normalized with respect to $\tau_0 = H_0\varepsilon_0/U$ which is 0.36 s and 0.24 s for U/U_{mf}=2 and 3, respectively.

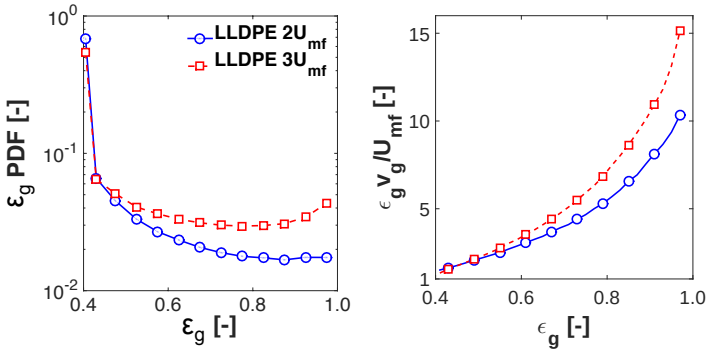

Figure 14: Time and spatially averaged PDF and the dependence of gas-flow on local void fraction for the fluidization of LLDPE particles at U/U_{mf}=2 and 3 in 50 cm diameter bed (H_0 = 50 cm).

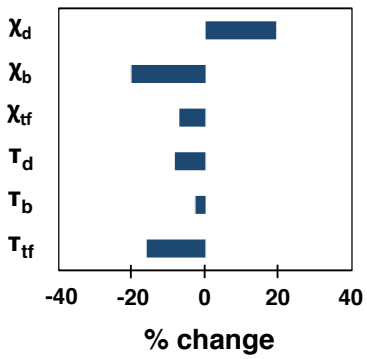

Figure 15: Sensitivity of gas distribution and residence times to threshold void fraction for bubble detection: percent change when $\varepsilon_{g,b}$ is increased from 0.7 to 0.8 for the fluidization of LLDPE particles at U/U_{mf}=3 in 50 cm diameter bed (H_0 = 50 cm).

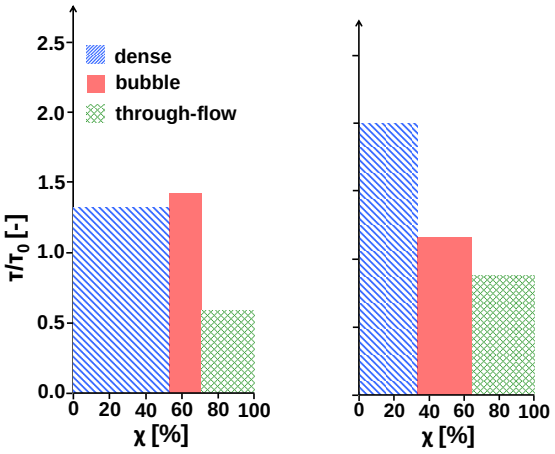

(a) Glass $2U_{mf}$ (b) Glass $3U_{mf}$

Figure 16: Residence time distribution of gas flow for fluidization of glass particles at U/U_{mf}=2 and 3 in 50 cm diameter bed (H_0 = 50 cm). All estimates are normalized with respect to $\tau_0 = H_0\varepsilon_0/U$ which is 0.48 s and 0.32 s for U/U_{mf}=2 and 3, respectively.

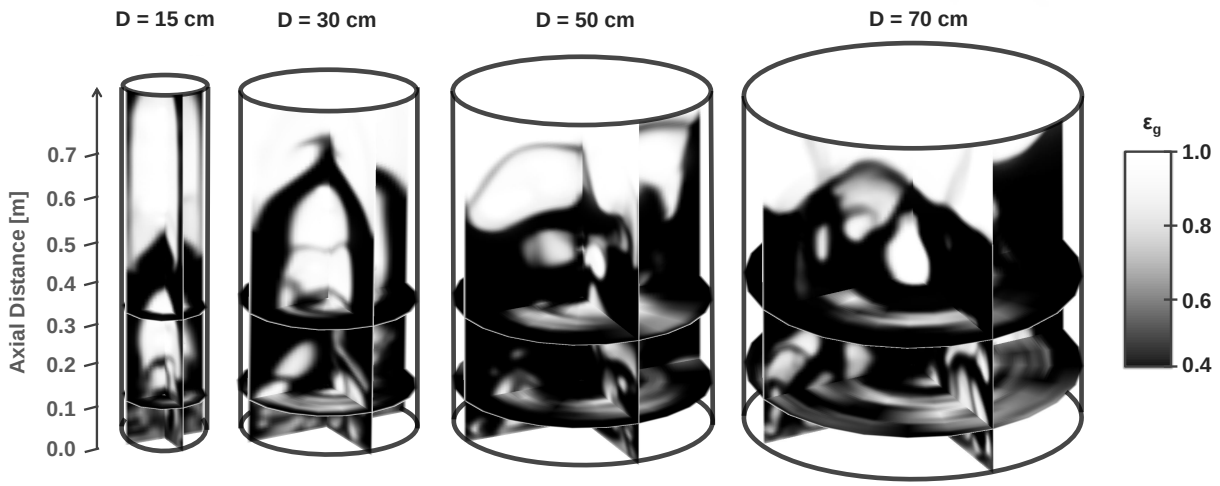

Figure 17: Instantaneous snapshots in different diameter (D = 15, 30, 50 and 70 cm) fluidized beds for fluidization of LLDPE particles at U/U_{mf}=3 (H_0 = 50 cm for all cases).

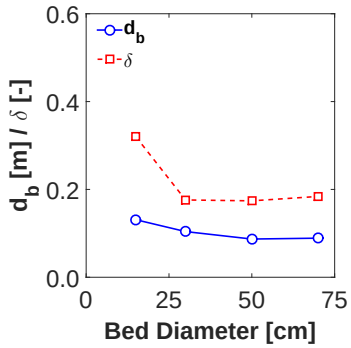

Figure 18: Time and spatially averaged bubble fraction and diameter in different sized fluidized beds (H_0=50 cm for all cases) for fluidization of LLDPE particles at U/U_{mf}=3. Statistics are computed in the bed interiors between y=10 cm and y=45 cm and bubble void threshold $\varepsilon_{g,b}$=0.7.

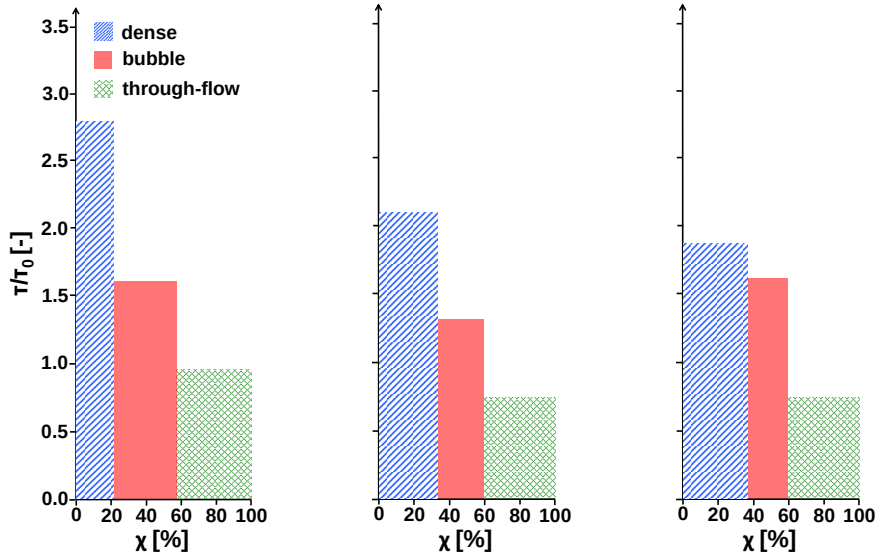

(a) D = 15 cm (b) D = 30 cm (c) D = 50 cm

Figure 19: Residence time distribution of gas flow for fluidization of LLDPE particles at U/U_{mf}=3 in 15, 30 and 50 cm diameter beds (H_0 = 50 cm). All estimates are normalized with respect to $\tau_0 = H_0\varepsilon_0/U$ which is 0.24 s.

Nomenclature

Main symbol definitions

A	cross-sectional area [m^2]
d_b	bubble diameter [m]
d_p	particle diameter [m]
δ	bubble fraction [-]
ε	void fraction [-]
$\varepsilon_{g,b}$	bubble threshold void fraction [-]
K	permeability [m^2]
Q	gas axial volume flow rate [m^3/s]
τ	residence time [s]
U	gas axial velocity [m/s]
U_b	bubble rise velocity [m/s]
U_{br}	isolated bubble rise velocity [m/s]
U_{mf}	minimum fluidization velocity [m/s]
χ	volume fraction of gas flow [-]

Main sub and super-scripts

b	bubble-phase
d	dense-phase
tf	throughflow-phase

Table 1: Summary of operating conditions

D [cm]	15-70	
H_0 [cm]	50	
U/U_{mf}	2-3	
Particles	Glass	LLDPE
d_p [mm]	0.50	1.15
ρ_m [kg/m^3]	2500	800
U_{mf} [m/s]	0.18	0.24

Table 2: Best-fit coefficient ϕ for correlating bubble velocity with diameter (Equation 12)

Particles	U/U_{mf}	ϕ	$\Delta U/U$
LLDPE	2	1.07	0.42
	3	1.33	0.50
Glass	2	0.93	0.40
	3	1.15	0.45